Earth Planet. Sci. Lett. 641 (2024) 118797

Contents lists available at ScienceDirect

Earth and Planetary Science Letters

journal homepage: www.elsevier.com/locate/epsl

Crustal and uppermost mantle structures of the North American Midcontinent Rift revealed by joint full-waveform inversion of ambient-noise data and teleseismic *P* waves

Bin He [a,g,*], Kai Wang [c], Tianshi Liu [b], Ting Lei [b], Nanqiao Du [b], Suzan van der Lee [d], Fiona Ann Darbyshire [e], Andrew Frederiksen [f], Hejun Zhu [g,h], David Lumley [g,h], Henry Halls [i], Qinya Liu [a,b]

[a] *Department of Physics, University of Toronto, Toronto, ON, Canada*
[b] *Department of Earth Sciences, University of Toronto, Toronto, ON, Canada*
[c] *School of Earth and Space Sciences, University of Science and Technology of China, Hefei, Anhui, China*
[d] *Department of Earth and Planetary Sciences, Northwestern University, Evanston, IL, USA*
[e] *Centre de recherche Geotop / Département des Sciences de la Terre et de l'atmosphère, Université du Québec à Montréal, Montréal, QC, Canada*
[f] *Department of Geological Sciences, University of Manitoba, Manitoba, MB, Canada*
[g] *Department of Geosciences, the University of Texas at Dallas, Richardson, TX, USA*
[h] *Department of Physics, the University of Texas at Dallas, Richardson, TX, USA*
[i] *Department of Earth Sciences, University of Toronto at Mississauga, Toronto, ON, Canada*

ARTICLE INFO

Editor: H. Thybo

Keywords:
The Midcontinent Rift
Continental underplating
Grenville orogeny
Ambient noise adjoint tomography
Teleseismic full waveform inversion

ABSTRACT

The Midcontinent Rift (MCR), hosting several world-class ore deposits, is the fossil remnant of a massive Mesoproterozoic rifting event (1.1 Ga) that did not lead to the formation of an ocean basin. To better understand the lithospheric processes associated with the rifting stage and its subsequent failure, we developed a novel full-waveform joint inversion method using ambient noise data and teleseismic *P* waves for this seismically inactive region. We apply this approach to three years (2011-2013) of seismic recordings from the Superior Province Rifting EarthScope Experiment (SPREE) (~12 km average station spacing) and the USArray Transportable Array (~70 km average station spacing), and obtain a new 3D high-resolution Vs model down to 100 km depth, as well as Vp and density models down to 60 km depth. The model shows major velocity anomalies in agreement with previous seismic studies for the western arm of the MCR. In particular, we observe high density (2.8-3.0 g/cm^3), Vp (6.3-6.5 km/s), and Vs (3.6-3.7 km/s) structures in the shallow upper crust within the rift, likely associated with volcanic rocks. Similar to a previously identified underplated layer, we also observe extensive normal-to-high Vs (3.8-4.2 km/s) along the whole rift axis and Vp (6.8-7.5 km/s) beneath the northern segment of the rift within the lower crust. However, the Vs and Vp values are lower than average for typical underplated materials. We suggest that this underplated layer may represent a combination of different intrusive rock types (e.g., gabbro, anorthosite) developed during magma differentiation processes, or contamination of the mafic magma by surrounding crustal material, or intrusions of sills.

1. Introduction

The Midcontinent Rift (MCR) hosts several types of world-class ore deposits and has been the focus of many geologic, geochemical, geochronologic and geophysical studies over the past several decades. It is the fossil remnant of a massive Mesoproterozoic rifting event (1.1 Ga) that did not lead to the formation of an ocean basin (Cannon, 1994). Filled with a thick layer of dense and highly magnetized volcanic rocks, it forms one of the most striking features on the gravity and magnetic anomaly maps of North America (Chase and Gilmer, 1973; King and Zietz, 1971). The tectonic setting of the MCR and environs is illustrated in Fig. 1. It presents an excellent case study on how and where such a rift forms and why it failed to develop into an oceanic spreading center as it evolved into the late stage of continental rifting. In addition,

* Corresponding author.
E-mail address: hebin14@mails.ucas.ac.cn (B. He).

https://doi.org/10.1016/j.epsl.2024.118797
Received 23 September 2023; Received in revised form 11 May 2024; Accepted 20 May 2024
Available online 19 June 2024
0012-821X/© 2024 The Author(s). Published by Elsevier B.V. This is an open access article under the CC BY-NC-ND license (http://creativecommons.org/licenses/by-nc-nd/4.0/).

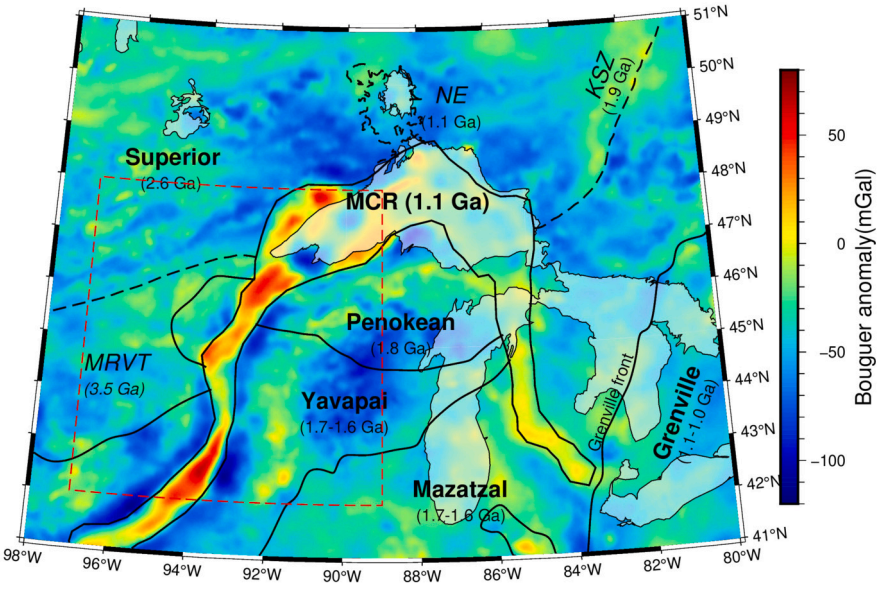

Fig. 1. Tectonic setting of the Midcontinent Rift (MCR) and environs overlain on the Bouguer anomaly map after Frederiksen et al. (2021). This area was assembled in the Proterozoic from a series of Archean cratons and later orogens. The oldest terrane is the ca. 3.5 Ga Minnesota River Valley Terrane (MRVT), which lies south of the largest Archean block, the ca. 2.6 Ga Superior Province. Post-accretionary deformation in the Superior was limited to uplift at ca. 1.9 Ga along a narrow region known as the Kapuskasing Structural Zone (KSZ) indicated by the black dashed line. A series of Proterozoic orogens were then accreted to the Superior, beginning with the Penokean orogens to the south ca. 1.8 Ga.; subsequent accretion of the Yavapai and Mazatzal orogens onto the southern Superior took place ca. 1.7–1.6 Ga. The Midcontinent Rift developed during a hiatus in orogenic activity on the margin (i.e. after the Shawinigan orogeny and before the Grenvillian orogeny) and then ceased extension contemporaneously with the onset of the Grenvillian orogeny ca. 1090 Ma, which is the most recent Proterozoic orogen, formed by the collision of Amazonia with Laurentia (Cannon, 1994; Swanson-Hysell et al., 2023).

the MCR has an unusual combination of the narrow form of a rift and a large volume of volcanic flows, two types of features that usually differ in geometry and origin (Stein et al., 2018). While a large number of geological, geochemical, geodynamic and geophysical studies have greatly improved our understanding of the structure and evolution of the rift (Behrend et al., 1988; Cannon, 1994; Vervoort et al., 2007; Miller et al., 2013; Shen et al., 2013; Yang et al., 2015; Zhang et al., 2016; Chichester et al., 2018; Bollmann et al., 2019; Frederiksen et al., 2021; Swanson-Hysell et al., 2021; Hodgin et al., 2022), the mechanisms behind the origin, evolution and subsequent failure of the rift are still under debate. The thermal perturbation of a mantle plume or hotspot has been proposed as the active origin of the rifting according to geochemical and isotopic studies of exposed igneous rocks related to the MCR (Davis and Green, 1997; Nicholson et al., 1997; White, 1997; Vervoort et al., 2007; Swanson-Hysell et al., 2021), whereas the far-field stresses related to the Grenville collisional events during the 1.09–0.98 Ga Grenville Orogeny (Rivers, 2008) have been invoked to support the hypothesis of passive rifting (McWilliams and Dunlop, 1978; Gordon and Hempton, 1986). Recently it was proposed that the voluminous volcanism of the MCR is the result of an elongated (linear) hydrous upwelling from the deep upper mantle, initiated by subducted hydrous oceanic lithosphere from the period that preceded the Shawinigan Orogeny (Swanson-Hysell et al., 2023).

The understanding of the lithospheric structure of the MCR and interpretations of its initiation mechanism and evolution history have benefited from numerous studies using geophysical data collected over the rift, including seismic data recorded by the USArray Transportable Array (TA) (Shen et al., 2013; Shen and Ritzwoller, 2016) and the Superior Province Rifting EarthScope Experiment (SPREE) (Zhang et al., 2016; Chichester et al., 2018; Bollmann et al., 2019). However, different data "see" quite different geophysical features of the lithospheric structures of the MCR. Long-period magnetotelluric (MT) data show that the western arm of the MCR is clearly evident in shallow depths (< 3 km), with a narrow resistive core flanked by elongate conductive basins (Yang et al., 2015). However, their resistivity anomalies associated with the MCR do not stand out at depths greater than 20 km. Seismic observations may provide better vertical resolution than gravity and magnetic data, and the MCR's dense volcanic rocks are detected by both seismic reflection (Behrend et al., 1988) and receiver function data (Zhang et al., 2016), which are sensitive to density and velocity contrasts. However, large scale regional tomography studies of ambient noise (Shen et al., 2013; Schmandt et al., 2015; Shen and Ritzwoller, 2016) reveal reduced phase and/or group velocities along the rift. Such reduced wavespeeds may reconcile with the high density of the volcanic rocks if the bulk and shear modulus of the volcanic rocks have a smaller contrast with the surrounding granitic crust. Longer-period, two-station phase velocity dispersion measurements (Foster et al., 2020) and teleseismic *P* wave tomography (Bollmann et al., 2019) did not convincingly reveal lithospheric structures that correlate with the MCR. Therefore, while crucial for providing more constraints on the geological interpretation of this failed rift, constructing fine-scale and consistent density and velocity models of the lithosphere in this region of the MCR remains challenging.

Different from traditional ray-based seismic tomography methods (Ritzwoller et al., 2002), full-waveform inversion techniques (FWI, sometimes interchangeably known as *adjoint tomography* in earthquake seismology) utilize numerical seismic wave simulations as the forward solver and, by constructing more accurate misfit gradients for 3D models (Liu and Tromp, 2006; Tape et al., 2009; Tromp et al., 2005), provide an effective technique for high-resolution mapping of subsurface structures in both exploration and earthquake seismology applications (Liu and Tromp, 2006; Tape et al., 2009; Virieux and Operto, 2009; Fichtner et al., 2009; Zhu et al., 2012; Krischer et al., 2018; Tromp, 2020). The empirical Green's functions extracted from ambient-noise data can be also used in FWI, which we call ambient noise adjoint tomography (ANAT). Many studies have demonstrated its potential in resolving more pronounced velocity variations in the lithosphere and uppermost mantle compared to tomographic methods based on ray theory (Chen et al., 2014; Zhu, 2018; Sager et al., 2020; Maguire et al., 2022). The lateral resolution of ANAT mostly relies on the station distribution. However, its vertical resolution is limited to shallow depths (less than ~50 km) due to the effective period bands used (e.g., 5-35

s). More recently, FWI of teleseismic high-frequency P waves (including direct and scattered waves) based upon hybrid methods, which we will refer to as *TeleFWI*, has been demonstrated to be capable of providing both high lateral and vertical resolution beneath dense linear arrays (Monteiller et al., 2015; Wang et al., 2016; Beller et al., 2018; Wang et al., 2021). Thanks to the full-waveform information of both direct and scattered waves on vertical and radial components, TeleFWI not only helps us to resolve small-scale local heterogeneities and sharp velocity discontinuities, but also gives us constraints on multiple parameters, such as density, Vp and Vs. However, this method usually relies on the coherence of scattered wavefields across densely spaced stations (e.g., ~10 km station spacing) to avoid spatial aliasing (Beller et al., 2018). Although Beller et al. (2018) demonstrated that additional stations from other coarser seismic networks can help to improve the lateral resolution of TeleFWI, its high resolution is mainly restricted to the dense array.

Taking advantage of complementary lateral and vertical sensitivities of surface waves and teleseismic body waves, Wang et al. (2021) applied joint FWI to study the lithospheric structures of central California based on alternating ANAT and TeleFWI iterations. However, the alternating inversion minimizes two independent objective functions in ANAT and TeleFWI, using independent misfit gradients for these two objective functions. As a result, optimization strategies such as conjugate gradient methods (Hestenes and Stiefel, 1952) or quasi-Newton methods including the Limited-memory Broyden–Fletcher–Goldfarb–Shanno algorithm (LBFGS) (Nocedal and Wright, 2006), essential to speed up the convergence of the inversion, cannot be used in this inversion process. More importantly, when models are updated with different step lengths (which could be obtained by line-search methods) separately in ANAT and TeleFWI, the inversion processes may be dominated by one particular dataset (Wang et al., 2021). To mitigate these problems, we propose a formal joint inversion method to minimize one combined objective function as a weighted sum of the objective functions used by ANAT and TeleFWI. The misfit gradients from ANAT and TeleFWI are directly computed for the joint objective function, so that advanced optimization methods may be applied to speed up the convergence. The effects of these two datasets can be balanced by applying proper weights between the misfits of ANAT and TeleFWI.

In this study, we first lay out the details of this joint FWI method for ambient noise and teleseismic body waves, which is then used to construct high-resolution models of crustal and uppermost mantle structures of the western arm of the MCR using both the dense SPREE array and the background USArray data. We compare our Vp, Vs and density models with other published results and discuss their implications for understanding the underlying geological processes associated with the MCR.

2. Methodology

2.1. Adjoint tomography

Since its first application in earthquake seismology a decade and a half ago, adjoint tomography (or FWI) has been extensively used to resolve fine-scale structures both in regional (Tape et al., 2009; Fichtner et al., 2009; Zhu et al., 2012; Wang et al., 2016, 2020; Zhu et al., 2020; Maguire et al., 2022) and global tomographic studies (Bozdağ et al., 2016; Lei et al., 2020). In adjoint tomography, to minimize the misfit function ϕ of traveltime or waveform differences between observed and synthetic data, misfit gradients that describe the linearized relationship between the perturbations of the misfit ($\delta\phi$) and model parameters, can be obtained based on full numerical simulations of seismic wave equations by

$$\delta\phi = \oint [K_\rho(\mathbf{m})\delta ln\rho + K_\alpha(\mathbf{m})\delta ln\alpha + K_\beta(\mathbf{m})\delta ln\beta] \quad , \tag{1}$$

where $K_\rho(\mathbf{m})$, $K_\alpha(\mathbf{m})$, $K_\beta(\mathbf{m})$ are the misfit gradients for density (ρ), Vp (α) and Vs (β), respectively (Tromp et al., 2005; Liu and Tromp, 2006). In this study, to iteratively update these model parameters, we use a line search method in conjunction with a gradient-based optimization algorithm, i.e., the Limited-memory Broyden–Fletcher–Goldfarb–Shanno algorithm (L-BFGS) (Nocedal and Wright, 2006), to decide the optimal step length for model updates at each iteration.

2.2. Ambient noise adjoint tomography (ANAT)

The phase-traveltime (shortened as "traveltime" hereafter) differences between the empirical Green's functions (EGFs) from ambient noise cross-correlations and synthetic Green's functions (SGFs) from point-force sources can be minimized by seeking optimal model parameters (i.e., density, Vp and Vs) with the adjoint method. In this study, we define the frequency-dependent traveltime misfit based upon the multi-taper method (Zhou et al., 2004) as

$$\phi^T = \frac{1}{2N}\sum_{i=1}^{N}\int_{-\infty}^{\infty} \| \frac{\Delta T_i(\omega,\mathbf{m})}{\sigma_i} \|^2 d\omega \quad , \tag{2}$$

where $\mathbf{m}$ is the model vector, $\Delta T_i(\omega) = T_i^{obs}(\omega) - T_i^{syn}(\omega)$ denotes the frequency-dependent traveltime difference between the ith pair of SGF and EGF, N is the total number of measurements and σ_i denotes uncertainties associated with each measurement. We note here that even though Vp and density could potentially be updated, the traveltimes of the ambient noise have almost no sensitivity to these two model parameters.

2.3. Teleseismic full-waveform inversion (TeleFWI)

Differently from traditional traveltime inversion, TeleFWI seeks to minimize the waveform differences between synthetic and observed data (i.e., teleseismic body waves including scattered waves). In this study, we use the following least-squares misfit function defined as

$$\phi^F = \frac{1}{2N}\sum_{i=1}^{N}\int_{t_1}^{t_2} \| u_i(t) * W(t) - d_i(t) \|^2 dt \quad , \tag{3}$$

where N is the number of measurements, $d_i(t)$ and $u_i(t)$ represent the observed data and corresponding synthetics, and $*$ denotes the time convolution operator. The time window $[t_1, t_2]$ is defined to isolate P and subsequent Ps waves and probably first-order multiples (Wang et al., 2016) from other phases to reduce imaging artifacts.

The source wavelet $W(t)$ is estimated and then convolved with synthetics (u_i) prior to waveform matching in order to mitigate the effects of the source signature and structure outside the simulation domain (Beller et al., 2018; Wang et al., 2021). More details about obtaining synthetics and source wavelet estimation $W(t)$ can be found in section 3.2.

2.4. Joint inversion of ANAT and TeleFWI

Taking advantage of complementary sensitivities of surface waves (in this case, from ambient-noise data) and teleseismic body waves, the joint inversion seeks to simultaneously minimize the cost functions of ANAT (ϕ^T) and TeleFWI (ϕ^F). The proposed cost function is defined as

$$\phi^J = \frac{1}{2}\left(\frac{\phi^T}{\phi_0^T} + \lambda\frac{\phi^F}{\phi_0^F}\right) \quad , \tag{4}$$

where ϕ_0^T and ϕ_0^F denote the misfits of ANAT (Eq. (2)) and TeleFWI (Eq. (3)) from the first iteration, respectively. By rescaling the misfit functions for these two different measurements, the cost function of the joint inversion is therefore dimensionless, which makes it possible to use λ to adjust the relative weights of these two datasets. In

this study, we set $\lambda = 1$ so that ANAT and TeleFWI cost functions contribute equally. We note here that although the misfit function is joined together as in Eq. (4), the adjoint gradient for each individual misfit function is computed independently. The joint misfit gradient in Eq. (4) is simply the weighted sum of the gradients for individual dataset as derived from Eqs. (2) and (3) as

$$K^J(\mathbf{m}) = \frac{K^T(\mathbf{m})}{\phi_0^T} + \lambda \frac{K^F(\mathbf{m})}{\phi_0^F} \quad . \tag{5}$$

As a result, the joint inversion is implemented through the following five steps:

a. Before the first iteration ($k = 1$), the initial model is set to be either a smoothed 1D reference model or a smoothed 3D model obtained from previous studies.
b. For the k'th iteration: apply ANAT to compute the traveltime misfits (Eq. (2)) EGFs and SGFs, as well as the corresponding misfit gradients, e.g., $K_\rho^T(\mathbf{m})$, $K_\alpha^T(\mathbf{m})$ and $K_\beta^T(\mathbf{m})$. Similarly, apply TeleFWI to obtain the least-squares waveform misfits (Eq. (3)) and the corresponding misfit gradients. If it is the first iteration, save the misfit functions ϕ_0^T and ϕ_0^F.
c. Calculate the misfit function and the misfit gradients for the joint inversion through the weighted sums of the two misfit values and gradients computed in the previous step according to Eqs. (4) and (5).
d. Precondition the joint misfit gradients (Wang et al., 2016, 2021) and calculate the optimal updating directions based upon techniques such as L-BFGS.
e. Perform a line search (Wang et al., 2021) to obtain the optimal step length. If the misfit reduction compared to the previous iteration is less than 2%, terminate the inversion to avoid data over-fitting. Otherwise, update the model to $m^{(k+1)}$, and restart again for the $(k+1)$'th iteration.

3. Application to seismic data from the western arm of the MCR

3.1. Data

In this section, we apply the joint inversion to image the lithospheric structures of the western arm of the MCR. In total, we have 120 virtual sources for ambient noise EGFs and 7 teleseismic events yielding teleseismic *P* waves (Fig. 2). 66 virtual sources come from three dense arrays (SN-SN', SS-SS' and SM-SM') of the Superior Province Rifting Earthscope Experiment (SPREE, XI) (van der Lee et al., 2011; Wolin et al., 2015), with an average station spacing of about 12 km. The other 44 virtual sources come from the Earthscope Transportable Array, and the US backbone network (TA) (Fig. 2) with an average station spacing of about 70 km, which are used to improve the lateral resolution of the study region. The ambient noise data last over three years with about one and half years' overlap among different networks, which makes it possible to combine data from these different station networks (Bensen et al., 2007). Moreover, the three dense arrays provide a high spatial sampling of teleseismic *P* scattered waves that are important for resolving small-scale structures beneath the array (Beller et al., 2018). Overall, the combination of these two networks provides excellent coverage for studying the detailed subsurface structures of the MCR. The data processing steps for ambient noise and teleseismic waves can be found in Text S1 and S2 in the supplementary materials.

3.2. Implementation of joint inversion

We perform forward and adjoint full wavefield simulations based on the open-source spectral element method (SEM) package SPECFEM3D_Cartesian (Komatitsch and Tromp, 2002; Peter et al., 2011), the details of which can be found in Text 3 in the supplementary materials. To robustly image the lithosphere without being biased by previous regional models, we construct an initial 1D model (Fig. S4) by smoothing the *AK135* reference model (Kennett et al., 1995) vertically by a Gaussian function with a full width of 10 km. Furthermore, in this study, the effect of surface topography (generally <400 m) is not considered in inversions for either ambient noise or teleseismic data because the variations of the topography are far smaller than the model resolution of our dataset. Nevertheless, another independent inversion was conducted using a 1D initial model (Fig. S4) constructed from the regional *EMCUS2016* model (Shen and Ritzwoller, 2016), in which topography is considered and the same inversion parameters are used. For the sake of simplicity, we denote the initial models obtained from *AK135* and *EMCUS2016* as *AKinit* and *EMCinit*, respectively. The constructed models arising from the joint inversion using *AKinit* and *EMCinit* as the initial models are denoted as *AKinv* and *EMCinv* (see more discussion in Section 3.3), respectively.

To measure the traveltime differences (Eq. (2)) for ANAT, we follow similar inversion procedures to those outlined in Wang et al. (2021). For each master station, we conduct one forward wavefield simulation for Rayleigh waves by placing a single vertical point source $\mathbf{f} = (0, 0, f_z)$ at the master station and treating all the other stations as receivers. The source wavelet is set to be a Gaussian wavelet with 1.2 s half duration. Here, only the vertical-component SGFs are recorded at receivers and used to compare with EGFs at four period bands (6-15 s, 10-20 s, 15-30 s, and 20-35 s). For the TeleFWI (Eq. (3)), we apply the highly efficient FK-SEM hybrid method to simulate the teleseismic wavefield recorded at stations (Tong et al., 2014). As mentioned in Section 2.3, to mitigate the source-side complications, we need to estimate a source wavelet $W(t)$ and convolve it with the synthetic teleseismic data prior to computing their waveform differences. In this study, the source wavelet estimation is realized by the following two steps: firstly, performing a time-domain deconvolution of teleseismic synthetics from data on the vertical component (Kikuchi and Kanamori, 1982), and secondly, estimating the source wavelet through a principal component analysis (PCA) (Hagen, 1982; Wang et al., 2021) (see more details for event *P1* in Fig. S3).

After measuring the traveltime (ANAT) or waveform (TeleFWI) differences, we obtain the corresponding adjoint sources based on the objective functions shown in Eqs. (2) and (3), respectively. These adjoint sources are injected at stations to calculate event misfit gradients for either teleseismic events or virtual sources at master stations (Eq. (1)). According to the joint objective function in Eq. (4), these two types of gradients are then normalized by (ϕ_0^T and ϕ_0^F) and summed based on Eq. (5). A preconditioner defined based on the square root of depth is applied to the joint gradient in order to reduce the impact of dominant surface sensitivities and accelerate the convergence of the inversion at greater depths. To reduce spurious high sensitivities at the sources and receivers, the misfit gradients are then smoothed with Gaussian functions with a radius of 20 km horizontally and 10 km vertically, which is gradually reduced to 10 km and 5 km along the horizontal and vertical directions after 8 iterations. The L-BFGS as well as a line-search are used to further speed up the convergence of the inversion (Nocedal and Wright, 2006). To investigate the effect of the joint inversion, we also conduct ANAT-only, TeleFWI-only and alternating inversion (Wang et al., 2021) from the same initial model for our study region. The parameters for data processing, kernel preconditioning, and line search are the same as those for the joint inversion.

3.3. Resolution tests

We conduct resolution tests to examine the resolution and robustness of our joint inversions. A checkerboard model in all three parameters (Vs, Vp and density) with anomalies of a radius of 20 km (about the wavelength of 6-sec S waves in the upper crust) and ±12% perturbations relative to the initial model (*AKinv*) is used to compute the synthetic data. To examine the resolution beneath these three dense arrays, in

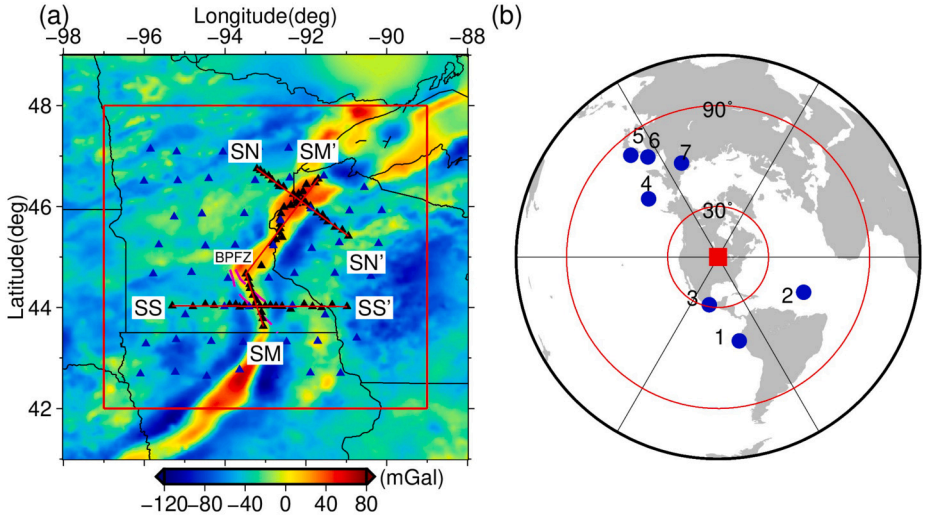

Fig. 2. (a) Bouguer anomaly map of the west arm of the Midcontinent Rift (MCR) and its surrounding region. The 120 seismic stations used in this study are indicated as triangles with blue triangles representing stations from the EarthScope USArray Transportable Array (TA) and the US backbone network and the black triangles representing the three dense arrays from the SPREE (XI) project. SN-SN' and SS-SS' are two profiles across the rift and SM-SM' is a profile along the rift. The magenta dashed lines indicate the Belle Plaine Fault Zone (BPFZ) (Sims, 1987). The region for which FWI inversions are performed is indicated by the red rectangle. (b) Locations of the seven teleseismic events used in TeleFWI are indicated as blue dots. The two red circles around the center of the study region (red square) denote the epicentral distance range between 30° and 90°. Details of the seven teleseismic events are summarized in Table S1 of the supplementary material.

particular the linear SN and SS arrays, the perturbations in the northern section are designed to be parallel to the SN array, while those in the southern section are parallel to the SS arrays (Fig. 3a). Synthetic EGFs and teleseismic *P* waves are computed for the same source-receiver geometries as used in the actual inversion. The synthetic teleseismic *P* waves are first convolved with the estimated source time function for the corresponding event to serve as "observed" teleseismic data. We then conduct joint inversion following the same procedures as in Section 3.2. Following the same inversion procedures, we also conduct the alternating inversion, and two separate inversions with only one of the datasets.

The left part of Fig. 3 displays the slices of recovered checkerboard models at depths of 20 and 80 km from the joint inversion. At the depth of 20 km, the inverted Vs perturbations (panel c) almost fully recover the checkerboard pattern (albeit with weaker amplitude), especially in the vicinity of the dense arrays thanks to the sensitivities from both ANAT and TeleFWI. The Vp and density perturbations also have reasonably good resolutions around the dense arrays mainly as a result of TeleFWI sensitivity. However, at the depth of 80 km, the resolutions of density, Vp and Vs are severely degraded compared to those at shallow depths and only some sensitivity is retained along the dense arrays, mainly for Vs and Vp. At this depth, the resolution of the Vp model is lower than the Vs model due to the longer wavelengths of transmitted *P* waves compared to the converted S waves, while the recovered density perturbations have much weaker amplitudes compared to both Vs and Vp models.

We also show vertical profiles of the recovered checkerboard model beneath the SN and SS dense arrays in the right panels of Fig. 3. From the recovered Vs profiles, it seems that the Vs model has a reasonably good resolution down to 100 km depth, although the resolution deteriorates slightly beneath 50 km depth. This is due to the fact that the ambient-noise data have very limited resolution beneath 50 km depth, and most sensitivity is due to teleseismic *P* waves and therefore is also subject to smearing along the teleseismic ray paths. The best resolutions for Vp and density are limited to the top ~40 km (Fig. 3). Again the vertical resolution for Vp is lower than Vs especially beneath 40 km depth due to the lower resolution of transmitted and scattered *P* waves compared to scattered S waves used to map Vs and density models.

We also examine the advantages of joint inversion for density, Vs, and Vp models compared to alternating inversions and single dataset inversions as shown in Figs. S13-S15. Another checkerboard test (with a perturbation radius of 12.5 km) is conducted to further show the resolution at even smaller scales where only TeleFWI is performed to save computational costs, as shown in Fig. S16. Combining the results shown in Figs. 3 and S16, we conclude that Vs has a reasonably good resolution down to 100 km depth and beyond, whereas reasonably good resolution for density and Vp extends to about 60 km depth. Two additional synthetic models are designed to further validate the reliability of the main features in our final models (next section), i.e., the positive anomaly in the upper crust and negative anomaly around the Moho (see more details in Text 4 of the supplementary materials). The corresponding inversion results demonstrate that our method is capable of recovering the target features in the upper and lower crust along different rift segments although with slightly weaker amplitudes.

3.4. Results

Fig. 4(a) shows the comparison of misfit reduction over iterations using different methods (e.g., ANAT-only, TeleFWI-only, alternating inversion). The misfit reduction from the joint or alternating inversion, compared with ANAT-only or TeleFWI-only inversions, seems to indicate a slightly slower convergence speed, which is not unexpected as joint inversions strive to fit both datasets at the same time. On the other hand, the ambient-noise misfit and teleseismic misfit from the joint inversion are reduced to similar levels as those from the ANAT-only and TeleFWI-only. Figs. 4(b-e) show the significant improvement of the traveltime misfit between the EGFs and SGFs from the final and initial models. We observe a reduction in both overall average traveltime anomaly and standard deviation for the final model (e.g., from -1.37 ± 1.24 s to -0.13 ± 0.74 s for the period band of 10-20 s). More detailed EGFs and SGFs waveform comparison for station pairs along three dense SPREE arrays, as well as the improvement of waveform fits for TeleFWI, can be found in Figs. S5 and S6, respectively. Figs. S7-S9 compare the slices extracted from the inverted models based on these four methods, which further demonstrates that the joint inversion manages successfully to balance two different datasets with complementary misfit gradients (ANAT and TeleFWI) while keeping a good convergence speed.

Next, we examine the main features in our final model, shown as model perturbations with respect to *AKinit* in Figs. 5 and 6 as horizontal

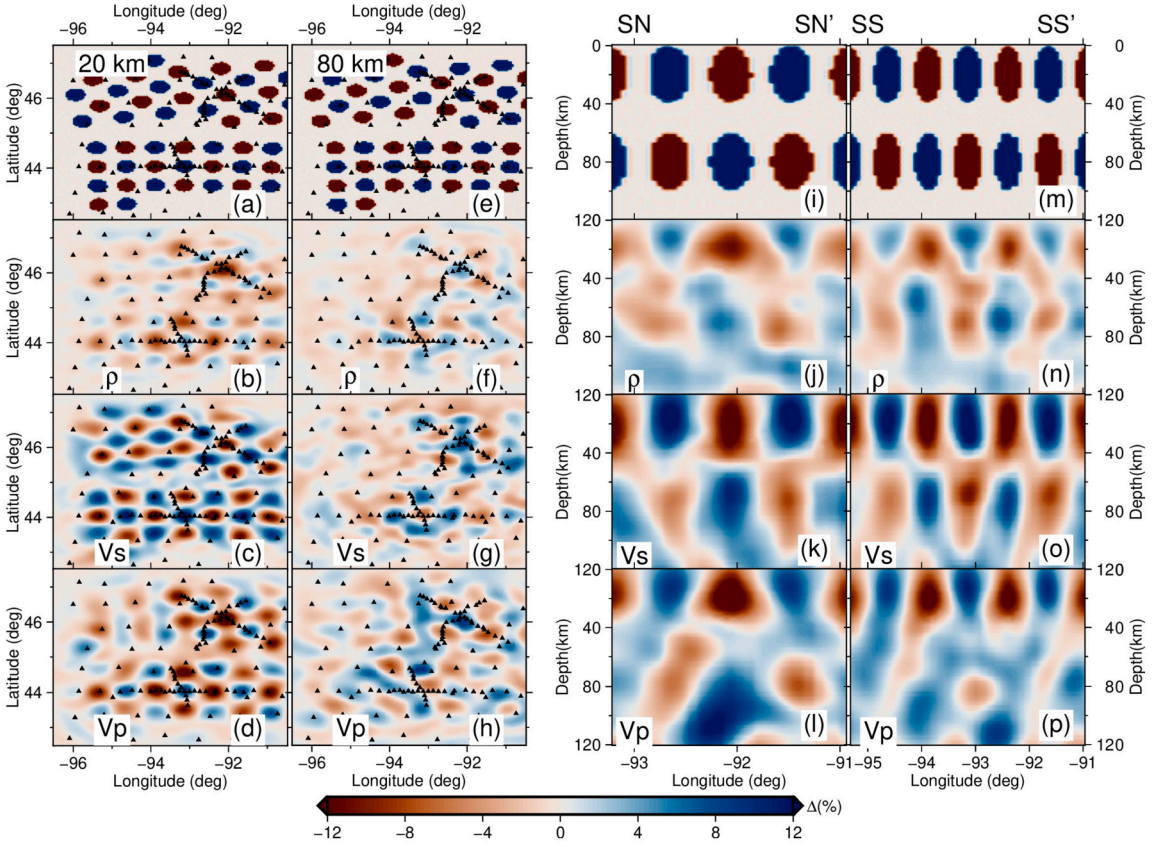

Fig. 3. Left: Resolution tests for the joint inversion shown as horizontal slices at the depths of 20 and 80 km with panels (a) and (e) showing the input model. Note that the polarity of the perturbations at 80 km is reversed relative to those at 20 km depth. The stations are shown with black triangles. Panels (b-d) show the recovered density, Vs and Vp perturbations at 20 km depth, while panels (f-h) show the recovered model perturbations at 80 km. Right: Vertical cross-sections extracted for SN-SN' and SS-SS' profiles. Panels (i) and (m) show the input models, while panels (j-l) and (n-p) show the recovered density, Vs and Vp perturbations.

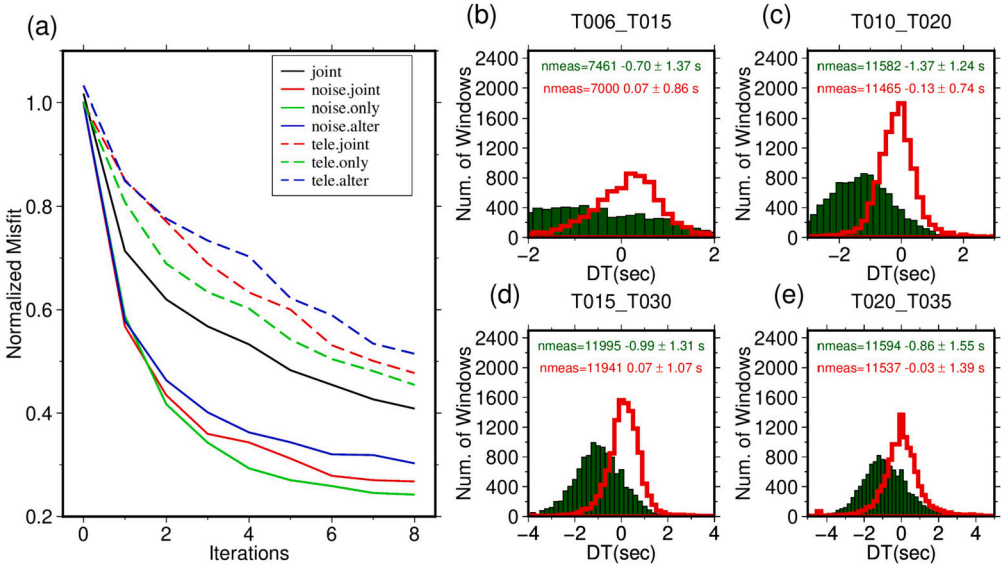

Fig. 4. (a) The misfit evolution of the full dataset in the joint inversion (solid black line), and the misfit reduction for the noise data (solid lines) and teleseismic waves (dashed lines) based on the joint inversion (red), alternating inversion (blue) and single-dataset-only inversion (green). Traveltime difference histograms between EGFs and SGFs for the initial (green) and final (red) model after the joint inversion are shown for four period bands: (b) 6-15 s, (c) 10-20 s, (d) 15-30 s and (e) 20-35 s. The number of measurements, average traveltime differences, and standard deviations for the initial (green) and final (red) model are provided in each panel. The change in histogram width and position for these four period bands clearly indicates a significant reduction in data misfit.

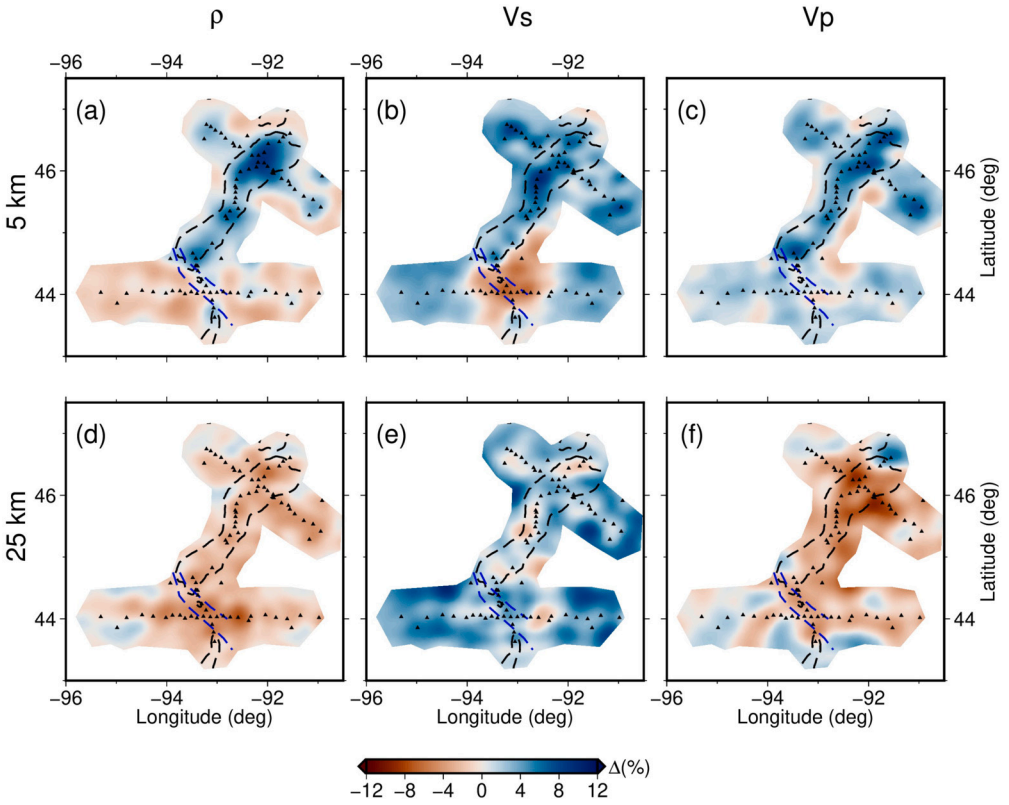

Fig. 5. Horizontal slices of density (panels a and d), Vs (panels b and f), and Vp (panels c and g) perturbations (i.e., (*AKinv-AKinit*)/*AKinit* × 100%) at the depths of 5 km and 25 km obtained from the joint inversion. The small black triangles in each panel represent the stations used in this study. The black dashed lines indicate the 0 mGal contour from the observed Bouguer anomaly (shown in Fig. 2) to highlight the center of the MCR, and the blue dashed line represents the Belle Plaine Fault Zone (Sims, 1987).

slices of density, Vs and Vp at depths of 5 km, 25 km, 50 km, and 80 km. We also show vertical cross-sections of absolute velocity and density values along three SPREE profiles (SN-SN', SS-SS' and SM-SM' in Fig. 2) in Fig. 7.

3.4.1. The upper crust

At the shallow depth of 5 km, the most prominent features in our final models are the positive anomalies in density, Vp and possibly Vs in the northern segment of the rift (Figs. 5a-c and 7). This high density, Vp and Vs feature in the upper crust may be correlated with other geophysical observables such as high Bouguer anomalies highlighted by the black dashed lines (0 mGal contours) in Fig. 5(a) and high density (between 2 and 25 km depth) inverted from observed Bouguer data and high-resolution seismic reflection profiles (Hinze et al., 1992). Deeper (5-30 km) buried volcanic rocks have been identified by the GLIMPCE seismic reflection profiles further north across Lake Superior (Cannon et al., 1989; Miller et al., 2013), including two reflection profiles (Profile A and B) in northwestern Wisconsin and eastern Minnesota (Chandler et al., 1989) that are close to our SN dense array (Fig. 2). Combined seismic and gravity modeling along these two profiles show similar density features as those in our results. On the other hand, this extensive high density, Vp and Vs feature could not be readily identified by other tomographic methods due to either sparse station coverage or limited sensitivity near the surface, particularly for Vp and density (Shen et al., 2013; Shen and Ritzwoller, 2016; Bollmann et al., 2019; Foster et al., 2020; Aleqabi et al., 2023).

In addition, and somewhat surprisingly, our new model reveals weak negative density anomalies and strong negative Vs anomalies in the southern segment of the rift around the center of the SS-SS' profile (Fig. 7). The weak negative densities beneath SS-SS' seem to be consistent with the pattern of gravity lows on either side of the gravity high at the rift axis observed at this locale (the solid line above Fig. 7b), which is a saddle point in the Bouguer gravity field. These flanking gravity lows may have been caused by deep horst-flanking sedimentary basins, which cannot be resolved by our model. The more strongly reduced S velocities correspond to a low S-velocity anomaly that in map view at a depth of 5 km roughly coincides with the Marshfield terrane (Fig. 6 in Whitmeyer and Karlstrom, 2007). Perhaps the Marshfield terrane has a lower rigidity or a distinct type of anisotropic fabric than the surrounding terranes of the Penokean and Yavapai Provinces (Whitmeyer and Karlstrom, 2007). These explanations would ascribe the observations to pre-existing terranes, of which our model does not reveal much given its tight focus around the MCR. Alternatively it is possible that these low Vs velocities are related to the post-rift bending and transpressional deformation this part of the rift experienced while rift-flanking faults to the north and south simply reversed their syn-rift normal faulting behavior to uplift the central horst after rifting ceased. Perhaps this combination of strike-slip with reduced reverse faulting left an upper crustal fabric with a lowered effective rigidity. In addition, modeling of gravity data combined with seismic reflection has suggested that the relatively uneroded sedimentary rocks near this location may grade laterally into a basaltic sequence toward the rift axis, which makes it difficult to detect the volcanic rocks by using active-source seismic data alone (Chandler et al., 1989) and could potentially lead to a reduced upper-crustal S velocity in our model.

While the resolution of the density model deteriorates significantly below 40 km depth (see Figs. 3 and S16 in the supplementary materials) and our method may not resolve the fine-scale density distribution in the top 5 km, we nevertheless still attempt to calculate synthetic Bouguer anomaly based on the final density model. Details on the calculation of synthetic Bouguer anomaly are outlined in Text 5 in the supplementary materials. As shown in Fig. 6(d), from the middle to the northern segment of the rift (44.5° N to 47° N), our synthetic Bouguer anomaly shows positive values (0 to +60 mGal) along the

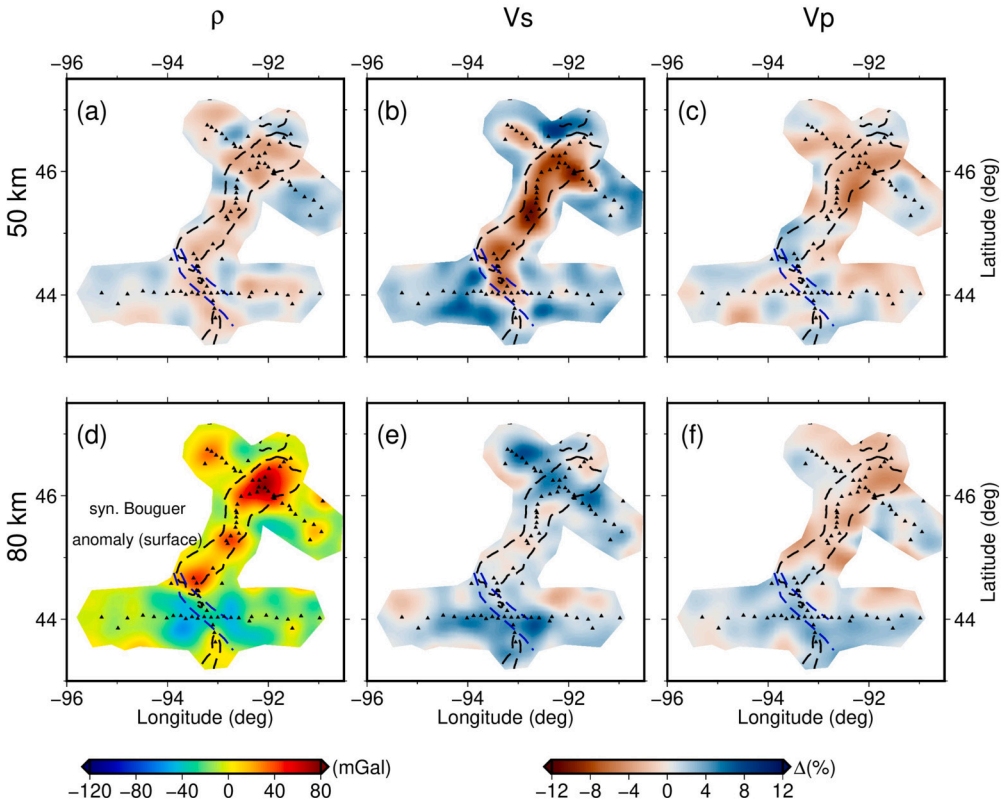

Fig. 6. Similar to Fig. 5 but for horizontal slices at the depths of 50 km and 80 km. Panel (d) shows synthetic Bouguer anomalies at the surface calculated based upon our final density model which reveal high gravity anomalies along the central (beneath SN array) and northern segment (beneath SS array) of the rift similar to those in the observed Bouguer data (Fig. 2a). For example, our synthetic Bouguer anomaly shows positive values (0 to +60 mGal) along the rift axis from 44.5° N to 47° N, while around 44° N, weaker negative values (-33 mGal) are flanked by stronger negative values (-38 to -44 mGal).

rift axis. It exhibits a high correlation with the observed Bouguer data (0 to +50 mGal) shown in Fig. 2. Along the southern segment of the rift (around 44° N), weaker negative values (-33 mGal) are observed to be flanked by stronger negative values (-38 to -44 mGal), similar to the observed Bouguer data, which also shows weaker negative values (-5 mGal) flanked by stronger negative values (-60 to -70 mGal). The amplitude differences between our synthetic and observed Bouguer anomalies are expected due to the resolution limitations of our data as well as the complexity of near-surface structures. Overall, our synthetic Bouguer anomaly shows a relatively higher gravity anomaly along the rift axis, which is generally consistent with observed Bouguer data.

On the top of each vertical cross-section profile shown in Fig. 7, we also show detailed comparisons of the synthetic and observed Bouguer anomaly data. The synthetic gravity profiles generally show similar magnitude of anomalies to observations, particularly the strong positive anomaly in the center of the SN-SN' profile (Fig. 7a) and along most of the northern segment of the SM-SM' profile which is a result of the high density values, 2.8-3.0 g/cm^3 in the upper crust compared to the standard value of 2.7 g/cm^3 (Wang et al., 2016). In the center of the SS-SS' profile, a significantly weaker negative Bouguer anomaly is observed to be flanked by stronger negative anomalies (Fig. 7b). However, the synthetic Bouguer anomalies are not strong enough to match the data and no strong positive density anomaly stands out directly beneath the rift.

3.4.2. *The mid-to-lower crust and the uppermost mantle*

At 25 km depth, our Vs model shows an extensive positive anomaly in the study region (Fig. 5e), which is most likely a result of the initial Vs model (*AKinit*) being slow in the mid-crust. It may explain the strong negative traveltime anomaly bias for the initial model in Figs. 4(b-e) and Fig. S5.

Another prominent feature in our Vs model is the normal-to-high Vs (3.8-4.2 km/s) compared with typical lower crustal rocks at depths of 40-60 km that above the Moho interface identified by the previous P/S receiver function study (Zhang et al., 2016). While our method is not sensitive to the exact depth of a sharp boundary such as the Moho, this extensive strong Vs anomaly along the rift (Fig. 6b) seems to be associated with the underplated layer identified from the P/S receiver functions (Zhang et al., 2016). We note here, this underplated layer seems neither a layer nor underplated and more of a frozen magmatic root. We also observe that these strong Vs features are generally continuous along the SM-SM' profile (Fig. 7l) except at the center of the profile due to the sparse station coverage traversing the cities of Minneapolis and St. Paul (see the station distribution in Fig. 2). The Vp and density do not show these distinct features in the mid-to-lower crust compared to the Vs, except for the northern segment of the rift (Figs. 7l). The general lack of Vp and density anomalies along the whole rift is consistent with the S-to-P receiver function results (Chichester et al., 2018) as well as Vp anomalies obtained from teleseismic *P* traveltime inversion (Bollmann et al., 2019). One possible reason is that the Vp structure is underestimated either due to the crustal underplating being complex in these sections of the rift (e.g., with strong lateral variations and steep dips) or that Vp and density have a lower resolution compared to Vs (Wang et al., 2016). However, synthetic tests from Chichester et al. (2018) and Bollmann et al. (2019), as well as ours shown in the resolution test in Section 3.3, all indicate that if there were extensive Vp anomalies in the lower crust, we would be able to detect them.

To further examine the robustness of the main features in our model, e.g., the high density and Vp structures along the northern segment of the rift (SN-SN' and SM-SM' profiles), and the low Vs structure around the southern segment of the rift (SS-SS' and SM-SM' profiles) in the upper crust; the extensive Vs perturbations at 40-60 km depth along the whole rift (SM-SM' profile), we experimented with a different initial model, *EMCinit* (Fig. S4 in the supplementary materials). *EMCinit* is a smoothed 1D model obtained from the *EMCUS2016*, a 3D shear-wave

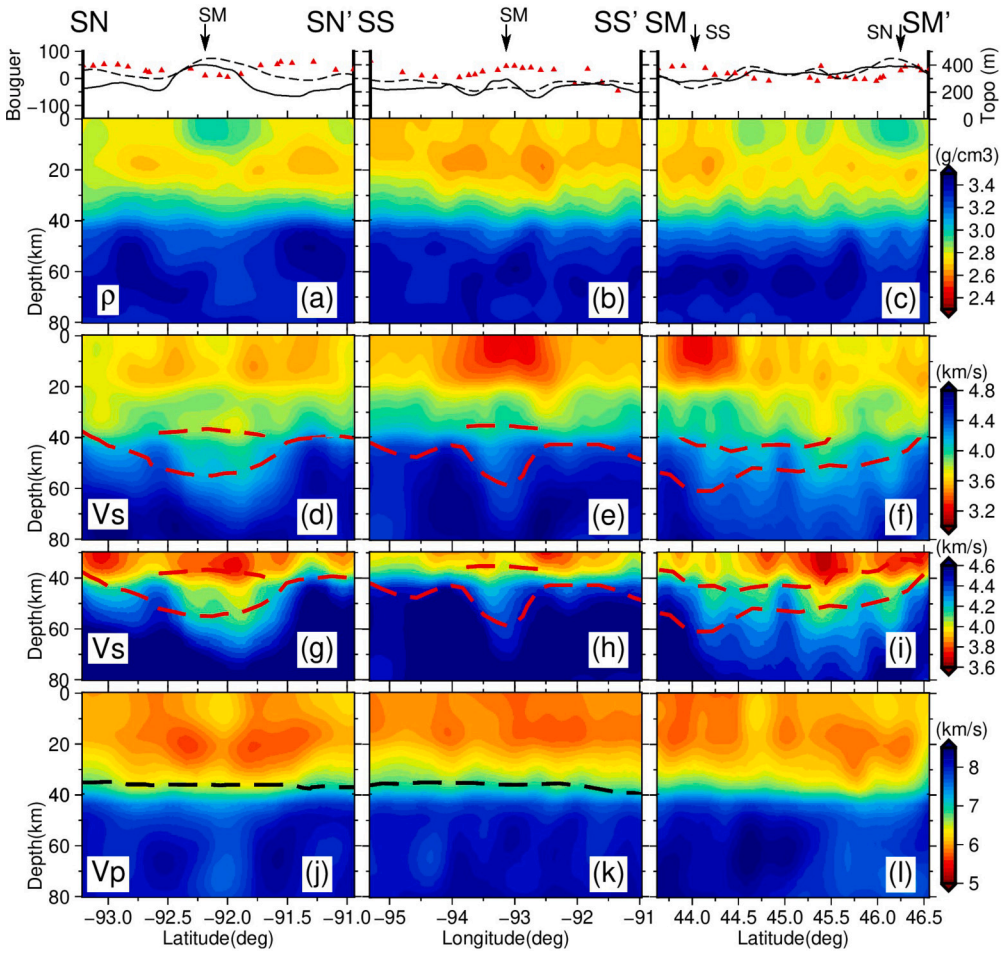

Fig. 7. Vertical cross-sections of absolute density (first row), Vs (second row) and Vp (fourth row) values for the final model, *AKinv*, along the SN-SN' (first column), SS-SS' (second column), and SM-SM' (third column) profiles. In the top panel, the corresponding observed and synthetic (calculated from the final density model) Bouguer anomalies along the three profiles are shown as black solid and dashed lines. The red triangles indicate the dense array along each profile with their vertical coordinates showing the variation of topography. The third row (Panels g, h, and i) are zoom-in of the Vs images in the second row around the Moho. The dashed red lines overlain on the Vs models represent the interfaces obtained from P-to-S receiver functions (Zhang et al., 2016), while the dashed black line overlain on the Vp model denotes the interfaces obtained from S-to-P receiver functions (Chichester et al., 2018). The cross points of the profiles are indicated by black arrows on top of the figure. The corresponding color bars are shown to the right of each row.

velocity model for the United States. It was constructed based on surface wave dispersion from ambient noise and earthquake data, Rayleigh wave H/V ratio, and receiver functions (Shen and Ritzwoller, 2016). After 8 iterations of joint inversion, we obtained another model, denoted as *EMCinv* in Figs. S10-S11. A detailed data match and model comparison along these three dense arrays is shown in Fig. S12. In general, the major velocity anomalies and contrasts of *EMCinv* have a good agreement with *AKinv*, as well as the calculated Bouguer anomalies from the obtained density model.

In summary, our models show major velocity anomalies and contrasts that are in general agreement with previous geophysical studies. In particular, we observe high density (2.8-3.0 g/cm^3), Vp (6.5-6.8 km/s) and Vs (3.6-3.7 km/s) structures in the shallow upper crust within the rift likely associated with the volcanic rocks. We also observe extensive anomalous Vs (3.8-4.2 km/s) and Vp (6.8-7.5 km/s) at 40-60 km depth in the northern segment of the rift, which we identify as a possible underplated layer.

4. Discussion

4.1. Dense volcanic rocks in the upper crust

The combination of seismic Vp, Vs and bulk density (as in this study) instead of a single parameter gives us a more comprehensive understanding of the rock types and physical properties of the MCR (Grauch, 2023). The relatively high density/Vp anomalies identified along the northern segment of the rift in Fig. 7(c) likely, and as expected indicate the existence of dense volcanic rocks in the upper crust. According to models from Chandler et al. (1989), Hinze et al. (1992) and Elling et al. (2022), the density of volcanic rocks for the MCR is likely in the range of 2.8 to 2.95 g/cm^3. Our final model shows that most of the northern segment of the SM-SM' profile has high-density values of 2.8-3.0 g/cm^3 in the upper crust. The corresponding Vp has values of 6.2-6.3 km/s. This combination of high density and Vp usually suggests a mafic composition for this region (Chandler et al., 1989; Grauch, 2023). Therefore, this high density/Vp/Vs feature likely represents volcanic rocks resulting from rift-related magmatism. Their current position arose through the contractional inversion stage of the MCR which juxtaposed them atop post-rift sedimentary rocks (Cannon, 1994; Vervoort et al., 2007; Miller et al., 2013). According to the latest geochronological evidence, the final inversion of the MCR might have occurred during the Rigolet phase of the Grenvillian Orogeny (Fig. 1) around 1,010–980 Ma (Hodgin et al., 2022; Swanson-Hysell et al., 2023).

4.2. Unusual underplated layer with low-to-average velocities?

Another prominent feature of our final model is the extensive anomalous Vs anomalies along the rift at depths of 40-60 km (Figs. 6

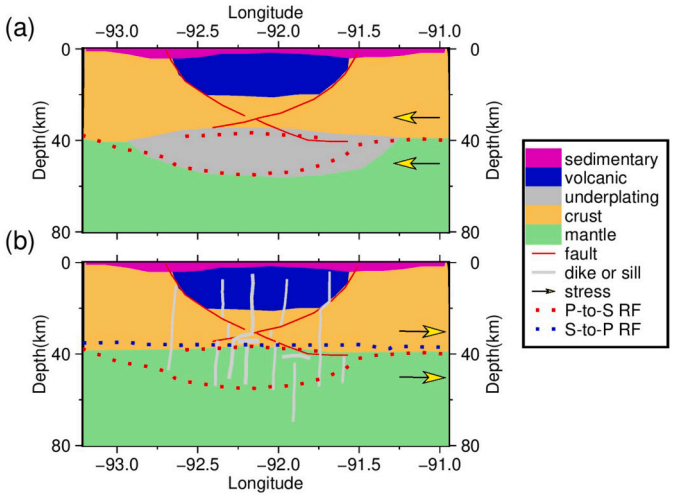

Fig. 8. Conceptual models created based upon the vertical cross-section of our final model *AKinv* beneath SN-SN' (Fig. 7) after Stein et al. (2015) and Elling et al. (2022). (a) The blue color indicates a sedimentary layer at the near-surface, the volcanic rocks in magenta color are bounded by faults with red lines. The underplated layer in gray color is well constrained by red dots which are from P-S receiver functions, basically consistent with our models. The yellow arrows denote the far-field compressive stress from the Grenvillian Orogeny. (b) If the Vs = 3.8-4.2 km/s layer is associated with the uppermost mantle rather than the lowermost crust, the Moho would be represented by the S-P (blue dots) and the upper P-S (red dots) receiver function signals. Feeder dykes (light gray vertical lines) intruded into the lowermost crust or uppermost mantle are used to interpret the anomalous Vs structures in our model. These could have been formed during the extension stage (yellow arrows) of the rift.

and 7). These are bounded by a pair of discontinuities identified by receiver function studies, which were interpreted as the top and base of an underplated layer in the lower crust (Zhang et al., 2016; Chichester et al., 2018). Similarly, magmatic underplating was also invoked to interpret the double bands of reflections at the base of the Moho dipping towards the rift center from the GLIMPCE seismic reflection profiles across the Lake Superior region (Behrend et al., 1988). Combined with gravity studies (Chandler et al., 1989; Elling et al., 2022), a conceptual model is illustrated in Fig. 8a under the assumption that the Moho beneath the MCR follows the bottom interface in the P-to-S receiver function study (Zhang et al., 2016). The gray color in the lower crust (Fig. 8a) indicates the region of the underplated material.

It has been hypothesized that due to the relatively low densities of crustal rocks, basaltic magmas in the continental plates are probably frequently trapped at or near the Moho within the lower crust, or in complex crust-mantle transition zones in a process known as continental underplating (Cox, 1993; Furlong and Fountain, 1986). This process may add high-density materials (e.g., mafic rocks) to the lower crust and uppermost mantle around the Moho. Therefore, it is valid to assume that the material also has high seismic velocity and Vp/Vs ratio compared to those of average continental crust (Thybo and Artemieva, 2013). Based upon petrological and experimental data, Furlong and Fountain (1986) estimated that the Vp for continental underplated material is likely in a range of 7.0-7.8 km/s on average. In addition, comparisons of seismic and xenolith data indicate that underplated materials are typically in the 7.0–8.0 km/s range for Vp and 4.0–4.6 km/s range for Vs, known as the 7.X or 4.X layers in continental North America (Schulte-Pelkum et al., 2017). Therefore, our Vp values of 6.8-7.5 km/s and Vs values of 3.8-4.2 km/s beneath the center of the SN profile seem to indicate an unusual underplated layer with low-to-average velocities compared to typical underplated materials. Furthermore, although at lower spatial resolution and at deeper depths, teleseismic *P* traveltime tomography by Bollmann et al. (2019) also identified a relatively low Vp imprint beneath the rift (compared to surrounding upper-mantle rocks) that could be related to the underplated layer. However, the Vp range of the underplated materials may vary among different tectonic settings and rock types. In particular, intrusions with different mafic and ultramafic compositions and variable cumulates may be present in the underplated material. For example, anorthosite has lower velocities and density (Christensen and Stanley, 2003) at Moho depths and could be responsible for the low-to-average velocities of our model.

In addition to high Vp, high Vp/Vs (>1.75) and Vs are also expected to be discriminators for identifying the underplated materials (Thybo and Artemieva, 2013). However, there are relatively few S-wave studies available. By setting an average Vp/Vs ratio to 1.75-1.8, Vs likely falls into the range of 4.0-4.4 km/s (4.X) for typical underplating materials. If this assumption is valid, our inferred Vs (3.8-4.2 km/s) at these depths further suggests an extensive underplated layer with low-to-average velocities compared to cratonic upper mantle but normal-to-high velocities compared to average continental crust, along the whole rift. Joint inversions of Rayleigh wave phase velocities and receiver functions (Shen et al., 2013; Shen and Ritzwoller, 2016; Aleqabi et al., 2023) and phase velocities measured by the two-station method (Foster et al., 2020) consistently indicate normal-to-high Vs values compared to typical lower crustal rocks, albeit with lower resolutions and higher lower-crustal Vs than our models. Based upon laboratory (Sui et al., 2022) and thermodynamic models (Hacker et al., 2015), Vs ranging between 3.8-4.2 km/s and Vp ranging between 6.8-7.5 km/s may correspond to about 45-55 $wt\%$ of SiO_2 component in the rock composition. Nevertheless, both our Vp and Vs indicate that the underplated materials are dominantly mafic in composition. The unusual lower-than-normal seismic velocities (Vs slightly lower than 4.X and Vp lower than 7.X) could either be the result of a combination of different rock types, e.g., gabbro and anorthosite, developed during magma differentiation processes or contamination of the mafic magma by surrounding crustal material (Grauch, 2023).

Although several scenarios were proposed to explain the voluminous volcanism of the MCR (Swanson-Hysell et al., 2023), it is generally agreed that there are three main magmatic stages during the development of the MCR: the early (ca. 1109-1106 Ma), latent (ca. 1106-1100 Ma) and main (ca. 1100-1084 Ma) stages (Vervoort et al., 2007; Swanson-Hysell et al., 2019, 2023). The early magmatic stage represents the initial pulse of magmatism in the MCR, where mafic melts intruding into the lower crust caused localized crustal heating and generation of silicic melts according to isotopic analysis (Vervoort et al., 2007). Although the ultimate cause of the latent stage is still unknown, one possible consequence is widespread crustal heating that may ultimately contribute to the partial melting of various components in the upper-and-mid crust as well as magma ponding near the Moho. In the main stage, voluminous basaltic lava flows migrate through the crust and erupt at the surface (Vervoort et al., 2007). The Duluth Complex, one of the largest mafic intrusive complexes on Earth, is a representative intrusion of this main stage of magmatic activity (Green, 1983; Vervoort et al., 2007; Swanson-Hysell et al., 2023). It is intriguing that the end of the main stage magmatism is temporally very close to the onset of the Ottawan phase (ca. 1090-1030 Ma) of the Grenvillian orogeny (Swanson-Hysell et al., 2019). Therefore, it has been suggested that the compressive stress (Fig. 8) from Grenvillian orogeny may have resulted in the cessation of the rift (Cannon, 1994; Swanson-Hysell et al., 2019). After that, the ponded magma around the Moho (underplated material) may have evolved into different mafic rock types and been contaminated with surrounding rocks at different depths, such as gabbro and anorthosite, during its cooling and solidification in the lower crust. Following subsequent thermal subsidence and inversion, the present-day underplated layer is situated at depths of 40-60 km along the rift. In addition, underplating during the latent and main magmatic stages may have played an important role in the tectonomagmatic evolution of the lithosphere, such as crustal thickening (Thybo and Artemieva, 2013).

4.3. Low velocities caused by the development of dikes?

Our interpretation of the lower crustal underplated layer partly depends on the location of the Moho. If we consider the top interface from both P-to-S and S-to-P receiver functions (Zhang et al., 2016; Chichester et al., 2018) as representative of the base of a normal unperturbed continental crust overlying a normal cratonic mantle, the anomalous material at 40-60 km depth beneath the rift is significantly slower than cratonic mantle. This comparison would be consistent, among others, with the relatively low phase velocities seen by Foster et al. (2020) at periods sensitive to this depth range. It is also known that basaltic magma may penetrate into the crust (Thybo and Artemieva, 2013) in the form of dikes and sills during the rifting process. According to geochronologic and geochemical analysis (Vervoort et al., 2007; Swanson-Hysell et al., 2019), older dykes (reversely magnetized) might have developed around the margins of the rift. Since all of the younger lava flows show normal polarity and exceed the volume of the reversely magnetized flows, it may be reasonable to assume that the younger feeder dykes are probably numerous and increase in numbers towards the center of the rift, provided that these vestiges of the crust are still preserved (maybe thinned and stretched at depth) beneath the rift's main volcanic zones. Based on this hypothesis, the low-velocity structures at 40-60 km depth along the rift seem to suggest that feeder dykes may be a dominant feature and have intruded into metamorphosed lowermost crust/uppermost mantle rocks, thus decreasing their velocities. However, the detection of radial anisotropy may provide key evidence for favoring the dyke hypothesis, and without it, their presence is quite speculative. Therefore, high-resolution seismic imaging of anisotropic structures beneath the MCR may help further address this question in the future.

5. Conclusion

We constructed a high-resolution Vs, Vp, and density model for the western arm of the MCR based upon a novel joint full-waveform inversion method using ambient noise and teleseismic waves recorded by both USArray and the SPREE array. By simultaneously fitting these two complementary datasets, the joint inversion provides significantly improved constraints on the subsurface structure with complementary lateral and vertical sensitivities and offers an efficient FWI method to map high-resolution structures beneath dense seismic arrays. The checkerboard tests show that beneath the SPREE array, the Vs structure can be reasonably well recovered down to ~100 km, Vp and density to ~60 km. The high-resolution lithospheric structures from our final models show velocity anomalies and discontinuities mostly in agreement with previous seismic studies. In particular, we observe high-density (2.8-3.0 g/cm^3), Vp (6.3-6.5 km/s), and Vs (3.6-3.7 km/s) structures in the shallow upper crust within the rift likely associated with the volcanic rocks. We also observe extensive normal-to-high Vs (3.8-4.2 km/s) along the rift axis, as well as normal-to-high Vp (6.8-7.5 km/s) beneath the northern segment of the rift in the lower crust. However, the Vs and Vp values are lower than average compared to typical underplated materials. We suggest that this lower crustal intrusion may represent a combination of different intrusive rock types, e.g., gabbro and anorthosite, formed during magma differentiation processes or contamination of the mafic magma by surrounding crustal material or intrusions of sills.

CRediT authorship contribution statement

Bin He: Writing – original draft, Validation, Software, Methodology. **Kai Wang:** Writing – review & editing, Software, Methodology. **Tianshi Liu:** Writing – review & editing, Software, Methodology, Investigation. **Ting Lei:** Writing – review & editing, Validation, Software, Formal analysis, Conceptualization. **Nanqiao Du:** Software, Methodology. **Suzan van der Lee:** Writing – review & editing, Visualization, Investigation. **Fiona Ann Darbyshire:** Writing – review & editing, Visualization, Validation, Formal analysis. **Andrew Frederiksen:** Writing – review & editing, Investigation, Formal analysis. **Hejun Zhu:** Writing – review & editing. **David Lumley:** Writing – review & editing. **Henry Halls:** Writing – review & editing, Visualization, Investigation. **Qinya Liu:** Writing – review & editing, Writing – original draft, Visualization, Validation, Supervision, Software, Resources, Project administration, Methodology, Investigation, Funding acquisition, Formal analysis, Data curation, Conceptualization.

Declaration of competing interest

The authors declare that they have no known competing financial interests or personal relationships that could have appeared to influence the work reported in this paper.

Data availability

Data will be made available on request.

Acknowledgements

We thank all the landowners that hosted a SPREE seismic station and service crews on their land for 2.5 years (http://www.earth.northwestern.edu/spree/Welcome.html and https://twitter.com/seismoSPREEDOM). These dense arrays make it possible for us to refine detailed lithospheric structures for the MCR and beyond. We also acknowledge all the work for developing the USArray (Transportable Array). All the SPREE data and USarray data are available at IRIS-DMC (http://ds.iris.edu/ds/nodes/dmc/data/). We also thank the developers of the software SPECFEM3D for their continued community work (https://github.com/geodynamics/specfem3d). In this study, we use the SPECFEM3D_Cartesian (version v2.0.2-3292-g7ab2414). Computations were performed on the Niagara supercomputer at the SciNet High-performance Computing (HPC) Consortium. SciNet is funded by the Canada Foundation for Innovation; the Government of Ontario; the Ontario Research Fund—Research Excellence; and the University of Toronto. B.H (before April 2022) and Q. L. are supported by the Natural Sciences and Engineering Research Council (NSERC) Discovery Grant 487237 and the J. Tuzo Wilson Research fund at the Department of Physics, University of Toronto. H. Zhu is supported by the U.S. National Science Foundation Grant number EAR 2042098. The figures are plotted by PyGMT (https://www.pygmt.org/latest/) which is originally based on GMT (Wessel et al., 2019).

Appendix A. Supplementary material

Supplementary material related to this article can be found online at https://doi.org/10.1016/j.epsl.2024.118797.

References

Aleqabi, G., Wysession, M., Wiens, D., Shen, W., Van der Lee, S., Darbyshire, F., Frederiksen, A., Stein, S., Jurdy, D., Revenaugh, J., 2023. Joint inversion of SPREE receiver functions and surface wave dispersion curves for 3-D crustal and upper mantle structure beneath the US Midcontinent Rift. J. Geophys. Res., Solid Earth 128, e2023JB026771.

Behrend, J., Green, A., Cannon, W., Hutchinson, D., Lee, M., Milkereit, B., Agena, W., Spencer, C., 1988. Crustal structure of the Midcontinent rift system: results from GLIMPCE deep seismic reflection profiles. Geology 16, 81–85.

Beller, S., Monteiller, V., Operto, S., Nolet, G., Paul, A., Zhao, L., 2018. Lithospheric architecture of the South-Western Alps revealed by multiparameter teleseismic full-waveform inversion. Geophys. J. Int. 212, 1369–1388.

Bensen, G., Ritzwoller, M., Barmin, M., Levshin, A.L., Lin, F., Moschetti, M., Shapiro, N., Yang, Y., 2007. Processing seismic ambient noise data to obtain reliable broad-band surface wave dispersion measurements. Geophys. J. Int. 169, 1239–1260.

Bollmann, T.A., van der Lee, S., Frederiksen, A.W., Wolin, E., Revenaugh, J., Wiens, D.A., Darbyshire, F.A., Stein, S., Wysession, M.E., Jurdy, D., 2019. P wave teleseismic traveltime tomography of the North American Midcontinent. J. Geophys. Res., Solid Earth 124, 1725–1742.

Bozdağ, E., Peter, D., Lefebvre, M., Komatitsch, D., Tromp, J., Hill, J., Podhorszki, N., Pugmire, D., 2016. Global adjoint tomography: first-generation model. Geophys. J. Int. 207, 1739–1766.

Cannon, W., Green, A.G., Hutchinson, D., Lee, M., Milkereit, B., Behrendt, J.C., Halls, H.C., Green, J.C., Dickas, A.B., Morey, G., et al., 1989. The North American Midcontinent rift beneath Lake Superior from GLIMPCE seismic reflection profiling. Tectonics 8, 305–332.

Cannon, W.F., 1994. Closing of the Midcontinent rift-A far-field effect of Grenvillian compression. Geology 22, 155–158.

Chandler, V.W., McSwiggen, P.L., Morey, G., Hinze, W.J., Anderson, R., 1989. Interpretation of seismic reflection, gravity, and magnetic data across middle Proterozoic Mid-Continent Rift system, northwestern Wisconsin, eastern Minnesota, and central Iowa. AAPG Bull. 73, 261–275.

Chase, C.G., Gilmer, T.H., 1973. Precambrian plate tectonics: the Midcontinent gravity high. Earth Planet. Sci. Lett. 21, 70–78.

Chen, M., Huang, H., Yao, H., van der Hilst, R., Niu, F., 2014. Low wave speed zones in the crust beneath SE Tibet revealed by ambient noise adjoint tomography. Geophys. Res. Lett. 41, 334–340.

Chichester, B., Rychert, C., Harmon, N., van der Lee, S., Frederiksen, A., Zhang, H., 2018. Seismic imaging of the North American Midcontinent Rift using S-to-P receiver functions. J. Geophys. Res., Solid Earth 123, 7791–7805.

Christensen, N.I., Stanley, D., 2003. Seismic velocities and densities of rocks. In: International Geophysics, vol. 81. Elsevier, pp. 1587–1594.

Cox, K.G., 1993. Continental magmatic underplating. Philos. Trans. R. Soc., Math. Phys. Eng. Sci. 342, 155–166.

Davis, D., Green, J., 1997. Geochronology of the North American Midcontinent rift in western Lake Superior and implications for its geodynamic evolution. Can. J. Earth Sci. 34, 476–488.

Elling, R., Stein, S., Stein, C., Gefeke, K., 2022. Three major failed rifts in central North America: similarities and differences. GSA Today 32, 4–11.

Fichtner, A., Kennett, B.L., Igel, H., Bunge, H.P., 2009. Full seismic waveform tomography for upper-mantle structure in the Australasian region using adjoint methods. Geophys. J. Int. 179, 1703–1725.

Foster, A., Darbyshire, F., Schaeffer, A., 2020. Anisotropic structure of the central North American craton surrounding the Mid-Continent Rift: evidence from Rayleigh waves. Precambrian Res. 342, 105662.

Frederiksen, A., Pokar, P., Barrow, E., Revenaugh, J., van der Lee, S., 2021. Altered mantle fabric beneath the Mid-Continent Rift. Geochem. Geophys. Geosyst. 22, e2021GC010012.

Furlong, K.P., Fountain, D.M., 1986. Continental crustal underplating: thermal considerations and seismic-petrologic consequences. J. Geophys. Res., Solid Earth 91, 8285–8294.

Gordon, M.B., Hempton, M.R., 1986. Collision-induced rifting: the Grenville Orogeny and the Keweenawan rift of North America. Tectonophysics 127, 1–25.

Grauch, V., 2023. Compressional-wave seismic velocity, bulk density, and their empirical relations for geophysical modeling of the Midcontinent Rift System in the Lake Superior region. Technical Report. US Geological Survey.

Green, J.C., 1983. Geologic and geochemical evidence for the nature and development of the Middle Proterozoic (Keweenawan) Midcontinent Rift of North America. In: Developments in Geotectonics. Elsevier., vol. 19, pp. 413–437.

Hacker, B.R., Kelemen, P.B., Behn, M.D., et al., 2015. Continental lower crust. Annu. Rev. Earth Planet. Sci. 43, 167–205.

Hagen, D.C., 1982. The application of principal components analysis to seismic data sets. Geoexploration 20, 93–111.

Hestenes, M.R., Stiefel, E., 1952. Methods of conjugate gradients for solving. J. Res. Natl. Bur. Stand. 49, 409.

Hinze, W.J., Allen, D.J., Fox, A.J., Sunwood, D., Woelk, T., Green, A.G., 1992. Geophysical investigations and crustal structure of the North American Midcontinent Rift system. Tectonophysics 213, 17–32.

Hodgin, E.B., Swanson-Hysell, N.L., DeGraff, J.M., Kylander-Clark, A.R., Schmitz, M.D., Turner, A.C., Zhang, Y., Stolper, D.A., 2022. Final inversion of the Midcontinent Rift during the Rigolet phase of the Grenvillian orogeny. Geology 50, 547–551.

Kennett, B.L., Engdahl, E., Buland, R., 1995. Constraints on seismic velocities in the Earth from traveltimes. Geophys. J. Int. 122, 108–124.

Kikuchi, M., Kanamori, H., 1982. Inversion of complex body waves. Bull. Seismol. Soc. Am. 72, 491–506.

King, E.R., Zietz, I., 1971. Aeromagnetic study of the Midcontinent gravity high of central United States. Geol. Soc. Am. Bull. 82, 2187–2208.

Komatitsch, D., Tromp, J., 2002. Spectral-element simulations of global seismic wave propagation—II. Three-dimensional models, oceans, rotation and self-gravitation. Geophys. J. Int. 150, 303–318.

Krischer, L., Fichtner, A., Boehm, C., Igel, H., 2018. Automated large-scale full seismic waveform inversion for North America and the North Atlantic. J. Geophys. Res., Solid Earth 123, 5902–5928.

Lei, W., Ruan, Y., Bozdağ, E., Peter, D., Lefebvre, M., Komatitsch, D., Tromp, J., Hill, J., Podhorszki, N., Pugmire, D., 2020. Global adjoint tomography—model GLAD-M25. Geophys. J. Int. 223, 1–21.

Liu, Q., Tromp, J., 2006. Finite-frequency kernels based on adjoint methods. Bull. Seismol. Soc. Am. 96, 2383–2397.

Maguire, R., Schmandt, B., Li, J., Jiang, C., Li, G., Wilgus, J., Chen, M., 2022. Magma accumulation at depths of prior rhyolite storage beneath Yellowstone Caldera. Science 378, 1001–1004.

McWilliams, M., Dunlop, D., 1978. Grenville paleomagnetism and tectonics. Can. J. Earth Sci. 15, 687–695.

Miller, J., Nicholson, S., Easton, R., Ripley, E., Feinberg, J., 2013. Geology and mineral deposits of the 1.1 Ga Midcontinent Rift in the Lake Superior region—an overview. In: Miller, J. (Ed.), Field Guide to the Copper-Nickel-Platinum Group Element Deposits of the Lake Superior Region. In: Precambrian Research Center Guidebook, vol. 13, pp. 1–49.

Monteiller, V., Chevrot, S., Komatitsch, D., Wang, Y., 2015. Three-dimensional full waveform inversion of short-period teleseismic wavefields based upon the SEM–DSM hybrid method. Geophys. J. Int. 202, 811–827.

Nicholson, S.W., Schulz, K.J., Shirey, S.B., Green, J.C., 1997. Rift-wide correlation of 1.1 Ga Midcontinent rift system basalts: implications for multiple mantle sources during rift development. Can. J. Earth Sci. 34, 504–520.

Nocedal, J., Wright, S.J., 2006. Numerical Optimization. Springer, NY.

Peter, D., Komatitsch, D., Luo, Y., Martin, R., Le Goff, N., Casarotti, E., Le Loher, P., Magnoni, F., Liu, Q., Blitz, C., et al., 2011. Forward and adjoint simulations of seismic wave propagation on fully unstructured hexahedral meshes. Geophys. J. Int. 186, 721–739.

Ritzwoller, M.H., Shapiro, N.M., Barmin, M.P., Levshin, A.L., 2002. Global surface wave diffraction tomography. J. Geophys. Res., Solid Earth 107, ESE-4.

Rivers, T., 2008. Assembly and preservation of lower, mid, and upper orogenic crust in the Grenville Province—implications for the evolution of large hot long-duration orogens. Precambrian Res. 167, 237–259.

Sager, K., Boehm, C., Ermert, L., Krischer, L., Fichtner, A., 2020. Global-scale full-waveform ambient noise inversion. J. Geophys. Res., Solid Earth 125, e2019JB018644.

Schmandt, B., Lin, F.C., Karlstrom, K.E., 2015. Distinct crustal isostasy trends east and west of the Rocky Mountain Front. Geophys. Res. Lett. 42, 10–290.

Schulte-Pelkum, V., Mahan, K.H., Shen, W., Stachnik, J.C., 2017. The distribution and composition of high-velocity lower crust across the continental US: comparison of seismic and xenolith data and implications for lithospheric dynamics and history. Tectonics 36, 1455–1496.

Shen, W., Ritzwoller, M.H., 2016. Crustal and uppermost mantle structure beneath the United States. J. Geophys. Res., Solid Earth 121, 4306–4342.

Shen, W., Ritzwoller, M.H., Schulte-Pelkum, V., 2013. Crustal and uppermost mantle structure in the central US encompassing the Midcontinent Rift. J. Geophys. Res., Solid Earth 118, 4325–4344.

Sims, P.K., 1987. Precambrian basement map of the northern mid-continent U.S.A. In: Rascoe Jr., B., Hyne, N.J. (Eds.), Petroleum Geology of the Mid-Continent. In: Tulsa Geological Society Special Publication, vol. 3, pp. 10–12.

Stein, C.A., Kley, J., Stein, S., Hindle, D., Keller, G.R., 2015. North America's Midcontinent Rift: when rift met LIP. Geosphere 11, 1607–1616.

Stein, S., Stein, C.A., Elling, R., Kley, J., Keller, G.R., Wysession, M., Rooney, T., Frederiksen, A., Moucha, R., 2018. Insights from North America's failed Midcontinent Rift into the evolution of continental rifts and passive continental margins. Tectonophysics 744, 403–421.

Sui, S., Shen, W., Mahan, K., Schulte-Pelkum, V., 2022. Constraining the crustal composition of the continental US using seismic observables. Geol. Soc. Am. Bull. 135, 2038–2056.

van der Lee, Suzan, Wiens, Douglas, Revenaugh, Justin, Frederiksen, Andrew, Darbyshire, Fiona, 2011. Superior province rifting earthscope experiment. https://www.fdsn.org/networks/detail/XI_2011/. https://doi.org/10.7914/SN/XI_2011.

Swanson-Hysell, N.L., Hoaglund, S.A., Crowley, J.L., Schmitz, M.D., Zhang, Y., Miller, J.D., 2021. Rapid emplacement of massive Duluth Complex intrusions within the North American Midcontinent rift. Geology 49, 185–189.

Swanson-Hysell, N.L., Ramezani, J., Fairchild, L.M., Rose, I.R., 2019. Failed rifting and fast drifting: Midcontinent Rift development, Laurentia's rapid motion and the driver of Grenvillian orogenesis. GSA Bull. 131, 913–940.

Swanson-Hysell, N.L., Rivers, T., van der Lee, S., 2023. The late Mesoproterozoic to early Neoproterozoic Grenvillian orogeny and the assembly of Rodinia: turning point in the tectonic evolution of Laurentia. In: GSA Memoir 220, Laurentia: Turning Points in the Evolution of a Continent. Geological Society of America.

Tape, C., Liu, Q., Maggi, A., Tromp, J., 2009. Adjoint tomography of the southern California crust. Science 325, 988–992.

Thybo, H., Artemieva, I., 2013. Moho and magmatic underplating in continental lithosphere. Tectonophysics 609, 605–619.

Tong, P., Komatitsch, D., Tseng, T.L., Hung, S.H., Chen, C.W., Basini, P., Liu, Q., 2014. A 3-D spectral-element and frequency-wave number hybrid method for high-resolution seismic array imaging. Geophys. Res. Lett. 41, 7025–7034.

Tromp, J., 2020. Seismic wavefield imaging of Earth's interior across scales. Nat. Rev. Earth Environ. 1, 40–53.

Tromp, J., Tape, C., Liu, Q., 2005. Seismic tomography, adjoint methods, time reversal and banana-doughnut kernels. Geophys. J. Int. 160, 195–216.

Vervoort, J.D., Wirth, K., Kennedy, B., Sandland, T., Harpp, K.S., 2007. The magmatic evolution of the Midcontinent rift: new geochronologic and geochemical evidence from felsic magmatism. Precambrian Res. 157, 235–268.

Virieux, J., Operto, S., 2009. An overview of full-waveform inversion in exploration geophysics. Geophysics 74, WCC1–WCC26.

Wang, K., Jiang, C., Yang, Y., Schulte-Pelkum, V., Liu, Q., 2020. Crustal deformation in southern California constrained by radial anisotropy from ambient noise adjoint tomography. Geophys. Res. Lett. 47, e2020GL088580.

Wang, K., Yang, Y., Jiang, C., Wang, Y., Tong, P., Liu, T., Liu, Q., 2021. Adjoint tomography of ambient noise data and teleseismic P waves: methodology and applications to central California. J. Geophys. Res., Solid Earth 126, e2021JB021648.

Wang, Y., Chevrot, S., Monteiller, V., Komatitsch, D., Mouthereau, F., Manatschal, G., Sylvander, M., Diaz, J., Ruiz, M., Grimaud, F., et al., 2016. The deep roots of the western Pyrenees revealed by full waveform inversion of teleseismic P waves. Geology 44, 475–478.

Wessel, P., Luis, J., Uieda, L., Scharroo, R., Wobbe, F., Smith, W.H., Tian, D., 2019. The generic mapping tools version 6. Geochem. Geophys. Geosyst. 20, 5556–5564.

White, R.S., 1997. Mantle temperature and lithospheric thinning beneath the Midcontinent rift system: evidence from magmatism and subsidence. Can. J. Earth Sci. 34, 464–475.

Whitmeyer, S.J., Karlstrom, K.E., 2007. Tectonic model for the Proterozoic growth of North America. Geosphere 3, 220–259.

Wolin, E., van der Lee, S., Bollmann, T.A., Wiens, D.A., Revenaugh, J., Darbyshire, F.A., Frederiksen, A.W., Stein, S., Wysession, M.E., 2015. Seasonal and diurnal variations in long-period noise at SPREE stations: the influence of soil characteristics on shallow stations' performance. Bull. Seismol. Soc. Am. 105, 2433–2452.

Yang, B., Egbert, G.D., Kelbert, A., Meqbel, N.M., 2015. Three-dimensional electrical resistivity of the north-central USA from EarthScope long period magnetotelluric data. Earth Planet. Sci. Lett. 422, 87–93.

Zhang, H., van der Lee, S., Wolin, E., Bollmann, T.A., Revenaugh, J., Wiens, D.A., Frederiksen, A.W., Darbyshire, F.A., Aleqabi, G.I., Wysession, M.E., et al., 2016. Distinct crustal structure of the North American Midcontinent Rift from P wave receiver functions. J. Geophys. Res., Solid Earth 121, 8136–8153.

Zhou, Y., Dahlen, F., Nolet, G., 2004. Three-dimensional sensitivity kernels for surface wave observables. Geophys. J. Int. 158, 142–168.

Zhu, H., 2018. Crustal wave speed structure of North Texas and Oklahoma based on ambient noise cross-correlation functions and adjoint tomography. Geophys. J. Int. 214, 716–730.

Zhu, H., Bozdağ, E., Peter, D., Tromp, J., 2012. Structure of the European upper mantle revealed by adjoint tomography. Nat. Geosci. 5, 493–498.

Zhu, H., Stern, R.J., Yang, J., 2020. Seismic evidence for subduction-induced mantle flows underneath Middle America. Nat. Commun. 11, 2075.